Environ. Sci. Technol. **2005**, *39*, 2867–2879

Longevity of Granular Iron in Groundwater Treatment Processes: Corrosion Product Development

TAMAR KOHN,[†] KENNETH J. T. LIVI,[‡]
A. LYNN ROBERTS,[†] AND
PETER J. VIKESLAND*,[†]

Department of Geography and Environmental Engineering, and Department of Earth and Planetary Science, 313 Ames Hall, Johns Hopkins University, 3400 North Charles Street, Baltimore, Maryland 21218-2686

Permeable reactive barriers employing iron as a reactive surface have received extensive attention. A remaining issue, however, relates to their longevity. As an integral part of a long-term column study conducted to examine the influence of inorganic cosolutes on iron reactivity toward chlorinated solvents and nitroaromatic compounds, Master Builder iron grains were characterized via scanning and transmission electron microscopy, electron energy loss spectroscopy (EELS), micro-Raman spectroscopy, and X-ray diffraction. Prior to exposure to carbonate solutions, the iron grains were covered by a surface scale that consisted of fayalite (Fe_2SiO_4), wüstite (FeO), magnetite (Fe_3O_4), maghemite (γ-Fe_2O_3), and graphite. After 1100 days of exposure to solutions containing carbonate, other inorganic solutes, and organic contaminants, the wüstite, fayalite, and graphite of the original scale partially dissolved, and magnetite and iron carbonate hydroxide ($Fe_3(OH)_{2.2}CO_3$) precipitated on top of the scale. Raman results indicate the presence of green rust (e.g., $[Fe_4^{2+}Fe_2^{3+}(OH)_{12}]$-$[CO_3{\cdot}2H_2O]$) toward the column outlet after 308 days of operation, although this mineral phase disappears at longer operation times. Grains extracted from a column exposed to a high concentration (20 mM) of sodium bicarbonate were more extensively weathered than those from columns exposed to 2 mM sodium bicarbonate. An iron carbonate hydroxide layer up to 100 μm thick was observed. Even though EELS analysis of iron carbonate hydroxide indicates that this is a redox-active phase, the thickness of this layer is presumed responsible for the previously observed decline in the reactivity of this column relative to low-bicarbonate columns. A silica-containing feed resulted in reduced reactivity toward TCE. Grains from this column had a strong enrichment of silicon in the precipitates, although no distinct silica-containing mineral phases were identified. The substitution of 2 mM calcium carbonate for 2 mM sodium bicarbonate in the feed did not produce a measurable reactivity loss, as the discrete calcium carbonate precipitates that formed in this system did not severely restrict access to the reactive surface.

Introduction

A number of contaminants, including chlorinated solvents, nitroaromatic compounds, and several metals and metalloids, can be readily removed from groundwater by iron-based permeable reactive barriers (PRBs) (*1*–*9*). At present, little is known about geochemical factors that dictate PRB longevity, a parameter that plays a key role in cost-effectiveness. Of particular concern are processes that lead to the precipitation of corrosion products on the iron grains, because the amount and identity of these precipitates may influence PRB performance. For example, the adsorptive and reductive precipitation behavior of contaminants such as arsenate or chromate has been shown to be strongly dependent on the mineral phase in question (*10*).

Some researchers (*11*–*14*) have suggested that the development of precipitates on the iron grains may reduce PRB reactivity over time. Recent studies postulate that graphite inclusions present within the iron matrix can act as reactive sites (*15*). Such inclusions might lose their activity if they became occluded by a thick layer of iron hydr(oxides) or other mineral phases. Several potential precipitates, however, such as magnetite (Fe_3O_4) (*16*–*18*) and green rust (e.g., $[Fe_4^{2+}Fe_2^{3+}(OH)_{12}][CO_3{\cdot}2H_2O]$) (*19*, *20*), as well as Fe^{2+} adsorbed onto iron (hydr)oxides (*16*, *21*–*24*), have been shown to reduce organic redox-active contaminants. This has led others to postulate that the formation of certain precipitate phases may serve to sustain PRB longevity (*25*).

In addition to these potential effects on surface reactivity, precipitate formation can also reduce the porosity of the iron matrix over time (*12*, *13*, *26*–*29*). To predict the magnitude of such porosity alterations from solution-phase measurements alone, the identity of the major precipitates must be known, as calculations based on different mineral phases lead to substantial differences in estimates of precipitate volume (*13*, *29*).

Geochemical models that take into account the formation of different mineral phases and their impact on the reactivity of the barrier media are potentially important tools in predicting PRB longevity (*30*). The accuracy of such models depends on the quality and completeness of the thermodynamic database as well as the validity of any kinetic assumptions made. To increase the utility of such models, an accurate understanding is needed as to how groundwater composition influences the identity of the precipitate phases that form.

Several researchers have attempted to characterize the surface precipitates generated in laboratory or field studies (*6*, *11*, *12*, *25*, *26*, *28*, *31*–*35*). The systems under consideration, however, varied considerably in iron type, contaminant identity, and solution composition, making it difficult to generalize the findings. In one noteworthy study, Furukawa and co-workers (*34*) investigated the precipitates found in two Peerless iron-based PRBs used to treat chlorinated solvents and hexavalent chromium. Using high-resolution transmission electron microscopy (TEM) and selected area electron diffraction (SAED), they found that the most common precipitates were ferrihydrite ($Fe_5HO_8{\cdot}4H_2O$) and a phase they identified as magnetite. Odziemkowski and co-workers, using in-situ Raman spectroscopy, determined that magnetite and possibly ferrous hydroxide ($Fe(OH)_2$) were the primary corrosion products, independent of solution composition (*32*). Similarly, Gui and Devine (*31*), using surface-enhanced Raman spectroscopy (SERS), found that the precipitate film consisted of $Fe(OH)_2$ and a mixture of Fe_3O_4 and γ-Fe_2O_3, regardless of the anions present in solution.

---

* Corresponding author phone: (540)231-3568; fax: (540)231-7916; e-mail: pvikes@vt.edu.
[†] Department of Geography and Environmental Engineering.
[‡] Department of Earth and Planetary Science.

10.1021/es048851k CCC: $30.25

A number of more highly oxidized precipitates have been encountered in column studies or PRBs exposed to solutions containing oxyanions such as Cr(VI) (*4*) or U(VI) (*12*, *33*), as well as in laboratory and field studies with aerobic groundwater (*12*, *26*). These precipitates include goethite (α-FeOOH), akaganeite (β-FeOOH), lepidocrocite (γ-FeOOH), hematite (α-Fe_2O_3), and amorphous iron (hydr)oxides (*4*, *11*, *12*, *33*). Commonly reported carbonate species include calcite ($CaCO_3$), aragonite ($CaCO_3$), carbonate green rust, and siderite ($FeCO_3$) (*6*, *11*, *12*, *33*−*35*). Unfortunately, although diffraction techniques and vibrational spectroscopy provide diagnostic information about these mineral phases, the identification of many secondary carbonate minerals is often postulated solely on the basis of thermodynamic arguments or visual analyses of SEM micrographs (*11*, *35*). As noted, a wide variety of surface precipitates have been detected in granular iron systems, but little is known about the temporal and spatial variability of these phases.

We previously reported (*9*) on long-term column experiments to investigate the influence of groundwater constituents on the reactivity of granular iron toward trichloroethylene (TCE). The experiments lasted up to 1100 days, and Master Builder iron was used as the reactive matrix. A somewhat shorter (475 days) column experiment was carried out using a reactive matrix consisting of 8% (w/w) albite admixed with the Master Builder iron, to assess the potential influence of aluminosilicate mineral dissolution and silica adsorption on the long-term reactivity of the iron. Results indicated that iron reactivity is dependent on feedwater composition and is a function of both column age and location within a column.

One of the main objectives of the present study was to systematically characterize precipitate formation as a function of solution composition, column age, and position within the columns, and to link this information to observed trends in reactivity. Four different techniques were employed: X-ray powder diffraction (XRD), electron microscopy (scanning and transmission electron microscopy), electron energy loss spectroscopy (EELS), and micro-Raman spectroscopy. These techniques were used because they provide complementary information, and thus their combined usage facilitates an improved overall understanding of precipitate formation. Although XRD and electron microscopy are well-established analytical tools for the study of mineral phases, EELS and micro-Raman spectroscopy have historically not been employed to the same extent. EELS was used to determine the oxidation state of iron in poorly characterized precipitates. Mineral identity was furthermore determined using micro-Raman spectroscopy. This technique enables the in-situ characterization of the corroded iron surface and corroborates the ex-situ analyses. To our knowledge, this is the first study to simultaneously utilize electron microscopy, EELS, and micro-Raman spectroscopy to examine iron corrosion product formation under carefully controlled laboratory conditions.

Experimental Section

Column Description. A comprehensive description of the column dimensions and operation, as well as a detailed account of the Master Builder iron matrix, can be found elsewhere (*29*). A schematic of the column setup is provided in the Supporting Information, Figure S1. In brief, a total of 10 Plexiglas columns (labeled A−J) containing a Master Builder iron matrix were operated for 1100 days (A−F) and 475 days (G−J), respectively. Column H contained a matrix composed of 8% (w/w) albite and 92% Master Builder iron, while the remaining columns contained 100% Master Builder iron. The columns were fed with anaerobic solutions of varying inorganic composition (see Supporting Information, Table S1) at a flow rate of 0.5 mL/min. The columns also received a mixture of 100 μM trichloroethylene (TCE) and 100 μM 1,2,3-trichloropropane (TCP), except for column F, which received a mixture of nitroaromatic compounds (2-nitrotoluene and either 4-nitroanisole or 4-nitroacetophenone). The columns were equipped with solid sampling ports near the influent, in the middle, and near the effluent of every column, through which grain samples were extracted.

Sampling Procedures. On days 288 (column F), 308 (columns G−J), 921 (column F), and the final day of column operation (day 1100 for columns B−F; day 475 for columns G−J), reacted iron grains were extracted from the solid sampling ports. The columns were first transferred to an anaerobic glovebox (5% H_2/95% N_2), before removing grains via the solid sampling ports and placing them into vials containing anoxic pore water obtained from the nearest liquid sampling port. The vials were sealed and stored in the glovebox until the grains were prepared for analysis. All analyses were completed within 1 month of sample extraction.

X-ray Diffraction (XRD). XRD measurements were obtained for samples from the influent end of columns B−J, as well as for untreated Master Builder iron grains. Several grains along with the accompanying pore fluid were removed from one of the vials, and within the anaerobic glovebox they were ground using a mortar and pestle until the overlying liquid attained an inky black and the grains a metallic color, indicating that substantial amounts of precipitates had been transferred from the iron grain into the liquid. The liquid was placed onto a low background silicon (400) wafer and was dried for several hours in the glovebox. Sample grinding and drying could potentially alter the mineral phases originally present at the grain surface. Such alterations, however, did not seem to occur in our samples, because the mineral phases detected by XRD on dried samples corresponded well to those detected by micro-Raman spectroscopy in the presence of pore water. The fresh Master Builder iron sample was ground after adding anoxic deionized (DI) water; this sample was then treated like the exposed samples. It has been suggested that this preparation procedure can lead to reduction of fully oxidized precipitates such as hematite and maghemite from the surface of the untreated iron grains (*25*), producing Fe^{2+} and a pure magnetite phase. The more highly oxidized phases may therefore be lost in the XRD analysis.

The samples were analyzed on a powder X-ray diffractometer model Philips XRG 3100, operated at 35 kV and 25 mA. The software package MDI Data Scan (Materials Data Inc., Livermore, CA 1995−1999) was used for data acquisition. Scans from $2\theta = 5{-}80°$ were obtained, where θ is the glancing angle between the beam and the sample. A Cu Kα anode was used as the radiation source ($\lambda = 1.54056$ Å). The scan rate was 0.05° and 15 s/step. The spectra were aligned to the background peak of the silicon wafer, which occurred at $2\theta = 69.13°$. The analysis software package Jade 3.1 (Materials Data, Inc., Livermore, CA 1991−97) and the reference database Powder Diffraction File 1994 (PDF-2 Database Sets 1−44, Dataware Technologies, Inc., 1985−94) were used to identify the mineral phases.

Electron Microscopy. Iron grain samples for scanning electron microscopy (SEM) analysis were rinsed with deoxygenated DI water, dried, and then removed from the glovebox. Between 3 and 5 grains from each sample were placed in copper cylinders and embedded in epoxy. The samples were polished and carbon coated to ensure their conductivity under the electron beam. A JEOL 8600 superprobe, equipped with energy dispersive spectroscopy (EDS) as well as wavelength dispersive spectroscopy (WDS), was used for digital backscattered electron (BSE) imaging and EDS and WDS X-ray mapping. The primary focus of this characterization process was on the precipitates located within deep pores. It was expected that these areas were more highly protected during sample preparation than the precipitates on the grain exterior. Several micrographs were taken of every sample, and EDS point analyses were performed at regions of interest. Compositional maps of selected regions were obtained at a magnification of 750× or more, using EDS for the elements Si, Ca, Mn, and Fe, and WDS for the elements O, S, Na, and Cl.

Regions of interest on the samples examined by SEM were identified and further investigated via transmission electron microscopy (TEM). Selected area electron diffraction (SAED) patterns, EDS analyses, and micrographs of chosen areas were obtained to identify the oxide phases present. A TEM sample was generated by impregnating several altered grains from the influent end of columns D and J in a 1 in. diameter mold. The grains were ground and polished to expose the metallic core. The polished surface was mounted on a glass slide with a temperature-sensitive adhesive, and the bulk of the sample was cut away with a trim saw. The remaining thin section was ground to a thickness of about 20 μm. The thinned sample was removed from the glass slide and glued onto a copper grid. The sample was then thinned to electron transparency in a Gatan Duo ion mill using a 6 kV beam, 1 μA current, and 18° milling angle. A 5 nm thick carbon coating was applied to the sample to reduce charging of the oxides and silicates.

The milled sample was placed in an FEI CM300 FEG TEM operating at 297 kV. This TEM has an ultimate point-to-point resolution of 0.18 nm and a beam diameter of around 0.2 nm. Selected area electron diffraction (SAED) patterns were obtained from areas of 100 nm or greater. The CM300 also has scanning transmission electron microscopy (STEM) capabilities, collecting transmitted beam and X-ray intensities generated by a rastered fine probe. X-rays were collected by an Oxford light element EDS detector and processed by an Emispec analyzer.

Electron Energy Loss Spectroscopy (EELS). EELS spectra were collected on milled samples by a Gatan GIF spectrometer in imaging mode (diffraction coupled) with a large beam diameter with a 10 μm objective aperture (semi angle of collection = 5 mrad), 2 mm entrance aperture, and a dispersion of 0.2 eV. Spectra were processed via the Gatan EL/P program for thickness correction and zero-loss deconvolution (*36*). The resolution of the detector is 1−1.5 eV over the several second acquisition times in these experiments.

Micro-Raman Spectroscopy. Samples for Raman spectroscopic analysis were prepared in an anaerobic glovebox by placing several grains into a cell containing 1−2 mL of porewater. The cell was sealed, removed from the glovebox, and multiple grains and multiple spots per grain were analyzed. In-situ Raman spectroscopic measurements were obtained using a Renishaw 1000 Raman microscope system. This instrument consists of an Olympus microscope, a single spectrograph fitted with holographic notch filters, and a thermoelectric cooled charge coupled device (CCD) detector. Sample excitation was achieved using the 632.8 nm line of a Melles Griot 35 mW HeNe laser. An objective lens with 50× magnification provided spatial resolution of 2 μm^2. Normal Raman spectroscopy (NRS) has a high penetration depth (~0.5−2 μm) that is a function of the material being probed (*25*, *37*). For the HeNe laser employed herein, NRS can be used to simultaneously probe multiple precipitate layers at a given location. Under these conditions, there is no vertical resolution and a mixed signal is acquired. Typically, 10−14 spectra over the range 200−2000 cm^{-1} were obtained for each sample (3−6 spots per iron grain for 2−3 grains). The collected spectra were analyzed using Grams/386 (ThermoGalactic Inc.; Salem, NH) spectral analysis software.

Results and Discussion

Characterization of Unreacted Master Builder Iron. The Master Builder iron used in field-scale PRBs is a low-grade cast iron (carbon content > 2%; ref *38*) that contains a number of chemical elements in addition to iron. These “impurities” include graphite inclusions (*39*, *40*), alloying metals (e.g., manganese, copper, chromium; ref *41*), metalloids (e.g., silicon), and nonmetals (e.g., phosphorus, sulfur) that either originate as residuals from the feedstocks used for the production of the iron (primarily spent automotive and industrial parts) or are purposely included to alter the stability of the final iron product (*41*).

When viewed via SEM in cross-section, unreacted iron grains exhibit a thin scale (<1000 nm) that completely covers the grain (Figure 1A). A close-up and compositional map of a pore leading from the surface of the grain to the interior is shown in Figure 1B. The pore is covered with a thin, confined oxide layer. Aside from the scale, the pores of the fresh iron grains were generally fairly clean and contained few precipitates. The compositional map shows that the oxygen content in the scale is higher than that in the iron core, indicating the presence of oxides. In addition, the pore boundary is marked by a greater amount of silicon as compared to the core. This enhanced silicon region marks the presence of fayalite in the scale, as determined by XRD (see below). The majority of the unreacted grains examined by SEM exhibited this well-defined, fayalite-containing boundary. We therefore define the fayalite/iron oxide scale as a marker of the grain boundary prior to contact with the feed solution. Any precipitates found beyond the fayalite-containing boundary formed during column operation.

Figure 1B also shows several MnS inclusions throughout the iron core. These inclusions can be recognized as regions of high sulfur (as shown) and manganese content (data not shown), and low iron density. Mn is often added to molten metal to form MnS inclusions that reduce the amount of sulfur in the bulk, thus altering the corrosion resistance of the final product. Recent studies examining the atmospheric corrosion of stainless steel (*42*) have shown that exposed MnS inclusions can act as preferential sites for the formation of corrosion pits. These inclusions could potentially serve as sites for the localized dehalogenation that has been reported on some of the iron types used for remediation (*43*).

XRD analysis of the surficial layer of the unreacted grains reveals the presence of wüstite, fayalite, and graphite (Figure S2). Diffraction peaks corresponding to either magnetite or maghemite are also present; these two minerals have very similar diffraction patterns and are difficult to distinguish using XRD alone (see Table S2 in the Supporting Information). Wüstite and magnetite are frequently the dominant phases in air-formed oxide scales, with wüstite the major phase formed at kiln temperatures above 700 °C (*44*, *45*). Fayalite presumably formed as a result of the high concentration of silica in Master Builder iron (~6.5%). This mineral typically forms at high temperatures (>1170 °C) in the presence of excess silicon (*44*−*46*). Graphite is also formed during the heating process, derived from organic residues such as oil or other contaminants on the iron filings, although it could also result from coke inclusions in the original preroasted iron. Graphite is found in nodules within the iron core, which extend into the scale (data not shown).

In an effort to distinguish between magnetite and maghemite, unexposed iron grains were characterized by micro-Raman spectroscopy. Comparison of the spectrum obtained (Figure 1C) to the band positions of relevant surface phases and solution components (Table 1) indicates that the unreacted iron was coated by a film composed of a mixture of magnetite, maghemite, and graphite. This surface com-

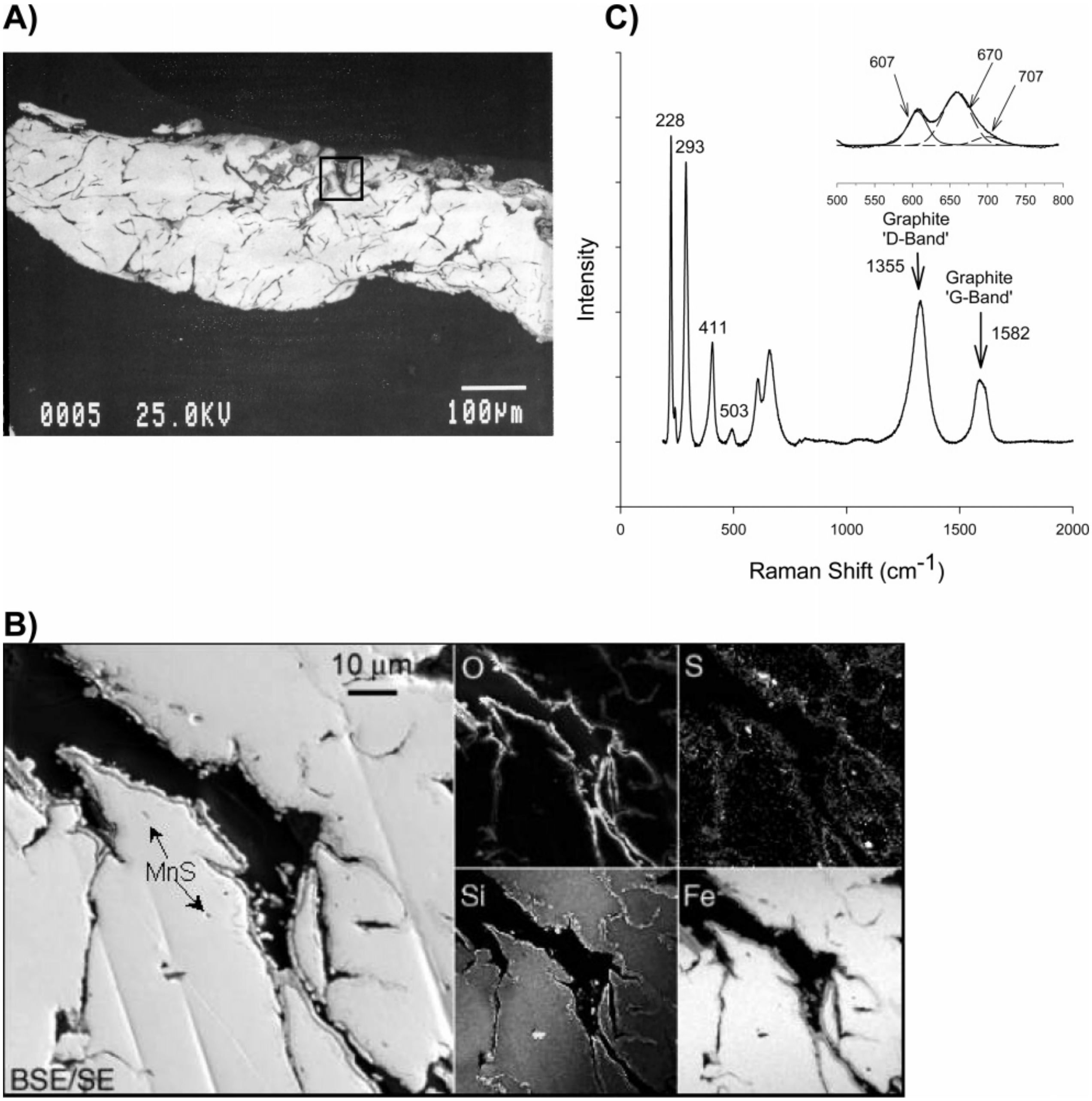

FIGURE 1. (A) SEM image of a cross-section through an untreated Master Builder iron grain. (B) Close-up on the indicated area of Figure 1A and elemental map of oxygen, iron, sulfur, and silicon. BSE/SE = backscattered/secondary electrons. Light colors indicate higher concentrations. (C) Raman spectrum from 180 to 2000 cm^{-1} of an unreacted Master Builder iron grain. Raman bands at 670 and 707 cm^{-1} (inset) correspond to magnetite and maghemite, respectively. Bands at 228, 293, 411, 503, and 607 cm^{-1} indicate the presence of hematite. As noted in the text, it is believed these peaks result from laser-induced thermal heating of magnetite. Both the ordered (G-band at 1582 cm^{-1}) and the disordered (D-band at 1355 cm^{-1}) bands for graphite are also apparent.

position is similar to that observed previously for Master Builder iron by micro-Raman techniques (*47*) and corroborates the XRD results. The presence of wüstite, which was detected by XRD, was not evident in the micro-Raman spectrum; the primary bands for this phase (616 and 652 cm^{-1}; ref *48*) may be overshadowed by the more intense bands for magnetite. Fayalite, detected by XRD, was not observed with micro-Raman spectroscopy. This absence may reflect the weak Raman scattering efficiency of fayalite overlain by layers of more abundant mineral phases. Raman bands corresponding to hematite are likely an artifact resulting from laser-induced thermal heating of magnetite (*49*, *50*). This is corroborated by the absence of hematite in the XRD spectra. We cannot, however, preclude the presence of hematite at concentrations below the XRD detection limit, or the autoreduction of hematite during the preparation of the unreacted grains for XRD analysis.

Evidence for the simultaneous existence of both magnetite and maghemite is provided by detailed analysis of the peak at ~670 cm^{-1} (inset of Figure 1C). Deconvolution of this composite band was necessary because the measured full width at half-maximum (FWHM) of 55 cm^{-1} was slightly larger than the reported range of FWHM values for magnetite (35–50 cm^{-1}; ref *51*). In accordance with published reports (*25*), when the FWHM value of the peak at ~670 cm^{-1} exceeds 50 cm^{-1}, we attribute the peak to reflect the simultaneous presence of the two phases. Peak deconvolution using Lorentzian/Gaussian peak forms indicates a high-intensity band at 670 cm^{-1} (consistent with expectations for magnetite; Table 1) and two sidebands at 607 and 707 cm^{-1} (the χ^2 value

TABLE 1. High Intensity Raman Bands of Selected Species in the 200−2000 cm^{-1} Region[a]

		Raman bands (cm^{-1})									refs
		Iron Oxides and Hydroxides									
hematite	α-Fe_2O_3	225	245	295	**415**	500	615	1320			83
goethite	α-FeOOH	225	244	**299**	**390**	420	480	550	1003		84
lepidocrocite	γ-FeOOH	**252**	380	526	650	**1307**					31
akagénite	β-FeOOH	400	**725**								62
ferrihydrite		370	510	**710**	134 0						85
maghemite	γ-Fe_2O_3	245	300	345	395	515	**645**	**670**	**715**	1440	83
magnetite	Fe_3O_4	294	319	415	540	**669**					51
	$Fe(OH)_2$	460	**550**								31
wustite	FeO	616	**662**								
green rusts											
Fe^{2+}−OH stretch of GR		**433**									60
Fe^{3+}−OH stretch of GR		**509**									60
interlayer CO_3^{2-} in GR		**1053**									60
interlayer Cl^-		**221**									66
		Carbonates									
siderite	$FeCO_3$	**289**	732	**1090**	1731						86
calcite	$CaCO_3$	**281**	712	**1088**	1436						86
aragonite	$CaCO_3$	**205**	704	**1085**							61
		Silicates									
albite	$NaAlSi_3O_8$	209	251	270	**291**	**479**	**510**	765	1100		87
fayalite	Fe_2SiO_4	**289**	369	505	562	**814**	**835**				88
am. silica	SiO_2	450	1050								87
		Aqueous Species									
carbonate	CO_3^{2-}	**1065**									89
bicarbonate	HCO_3^-	**1015**									89
Fe^{3+}−OH_2 in $[Fe(H_2O)_6]^{3+}$ (A_{1g})		496									89
Fe^{3+}−OH_2 in $[Fe(H_2O)_6]^{3+}$ (E_g)		456									89
Fe^{2+}−OH_2/Fe^{2+}−OH in $[Fe(H_2O)_6]^{2+}$ (E_g)		430									89
		Carbon Compounds									
graphite	G-band	**1582**									90
	D-band	**1355**									90

[a] Raman band locations are highly subject to instrument type and calibration, and thus some band assignments may differ by ±10 cm^{-1} from those listed in this table. Bold numbers reflect the most intense Raman bands.

for the fit was equal to 1.27; alternate fits obtained using either one or two bands were less successful in replicating the peak shape). The sideband at 707 cm^{-1} indicates the presence of maghemite (γ-Fe_2O_3; Table 1); this peak position is slightly shifted from that listed in Table 1, but is consistent with reports in the literature (*51*). Raman band positions often vary by ±10 cm^{-1} depending on the instrument employed and its calibration.

In the presence of oxygen (*52*, *53*) or aqueous oxidants (e.g., Cr(VI), refs *54*, *55*; Ag(I), ref *56*; carbon tetrachloride, refs *57*, *58*), magnetite may undergo topotactic oxidation to produce maghemite, as illustrated for dissolved oxygen:

$$3Fe_3O_4 + {}^1/_2O_2 + 2H^+ \rightarrow 4\gamma\text{-}Fe_2O_3 + Fe^{2+} + H_2O \quad (1)$$

This process results in the formation of a maghemite crust at the fluid−particle interface. If further magnetite oxidation is to proceed once this coating forms, interstitial Fe^{2+} must diffuse to the surface to maintain charge electroneutrality (*52*, *53*, *56*, *59*). For large particles, such as the iron grains, significant quantities of interstitial Fe^{2+} are diffusively unavailable (*60*), and thus magnetite and maghemite are often found together. The relatively large sampling depth of Raman spectroscopy enables measurement of both surficial maghemite and underlying magnetite.

Spatial and Temporal Variability of Precipitate Phases. Representative Raman spectra of iron grains obtained from column G (fed with 100 μM TCE/100 μM TCP/2 mM $CaCO_3$ at pH 7.5) on day 288 are shown in Figure 2. Comparison of the spectra indicates the interfacial composition of the grains changed significantly between the inlet and the outlet of the column. For grains extracted near the inlet (port 1), Raman bands corresponding to magnetite (peaks at ~670 and ~550 cm^{-1} are the A_{1g} and the T_{2g} modes, respectively), maghemite (see inset − peaks at 645 and 705 cm^{-1}), and surface associated carbonate (1069 cm^{-1}; ref *60*) are clearly evident. Also apparent is a broad peak between 250 and 350 cm^{-1}. This peak, which is probably a composite of a number of overlapping Raman bands, does not correspond to any knowniron (hydr)oxides or carbonates, but was observed in

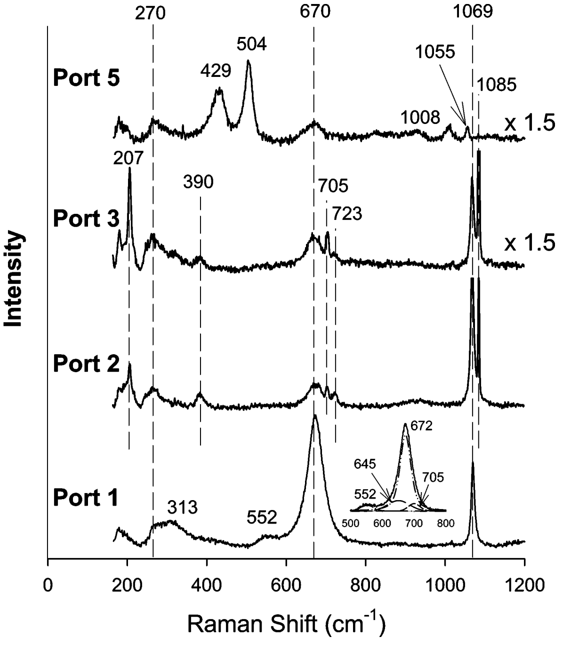

FIGURE 2. Raman spectroscopic results for a column fed with a $CaCO_3$/CO_2 buffered solution at pH 7.5. As shown by the changes in the band positions, the composition of the surface precipitates changes significantly between the influent (port 1) and effluent (port 5) ends of the column. The identity of the predominant surface precipitates at a given port is given in Table 2.

TABLE 2. Mineral Phases Identified by Raman Spectroscopy for Columns F−J as a Function of Operation Time and Position within a Given Column[a]

column	port 1	port 2	port 3	port 4	port 5
F (day 308)	magnetite	magnetite green rust			
F (day 921)	magnetite goethite	magnetite goethite			
G	magnetite maghemite	magnetite maghemite aragonite goethite	magnetite aragonite goethite		magnetite green rust
H	magnetite maghemite goethite	magnetite goethite	magnetite lepidocrocite	magnetite lepidocrocite	magnetite green rust
I	magnetite maghemite goethite	magnetite goethite	magnetite	magnetite lepidocrocite green rust	magnetite lepidocrocite green rust
J	magnetite maghemite	magnetite maghemite	magnetite green rust	magnetite green rust	magnetite green rust

[a] These phases were detected at the iron−water interface in at least 4 of the 12 spectra obtained for each sample.

all of the aged samples examined via micro-Raman spectroscopy.

For iron grains extracted from ports ∼30 and ∼80 mm from the inlet, additional major peaks at 207, 705, and 1085 cm^{-1} are observed. These peaks indicate the presence of aragonite ($CaCO_3$), with the peaks corresponding to the $E_{g,ext}$, $E_{g,int}$, and A_{1g} modes of the carbonate anion within the crystal lattice, respectively (*61*). Were calcite present instead of aragonite, we would have expected a strong Raman band at 281 cm^{-1}. The formation of aragonite instead of calcite in granular iron systems is consistent with modeling studies on the geochemistry of a PRB (*30*) and with previous Raman measurements (*32*). As discussed below, samples from the same column subjected to XRD analysis indicate that calcite was the predominant carbonate mineral phase in this column after 475 days. Near the column outlet (port 5), the peaks corresponding to aragonite and surface associated carbonate disappear, and major peaks at 429, 504, and 1055 cm^{-1} appear. The peaks at 429 and 504 cm^{-1} are typically considered to be characteristic of the Fe^{2+}−OH and Fe^{3+}−OH stretches, respectively, of green rust compounds (*60*, *62*, *63*). Green rusts, mixed valence Fe^{2+}−Fe^{3+} layered double hydroxide compounds of the pyroaurite class (*64*), have previously been observed as iron corrosion products (*60*, *62*, *63*, *65*, *66*). Raman spectroscopy enables identification of the interlayer ions of green rust, as the Cl^-, CO_3^{2-}, and SO_4^{2-} species present within the interlayer exhibit characteristic Raman shifts (interlayer Cl^- ∼220 cm^{-1}, ref *66*; interlayer CO_3^{2-} ∼1053 cm^{-1}, refs *60*, *63*) that differentiate them from noninterlayer species. Within the columns, both carbonate (present in the feed solutions) and chloride (a product of the dechlorination reactions) are present and have the potential to be found within the interlayer. From the spectrum depicted in Figure 2 for grains extracted from port 5 of column G, it is apparent that a peak at 1055 cm^{-1} exists, and we attribute this to the presence of carbonate within the interlayer.

Evaluation of the FWHM for the Raman band at ∼670 cm^{-1} for grains extracted from ports 2, 3, and 5 suggests that maghemite was not present within the distal portions of this column. At each port, the average measured FWHM value was ∼45 cm^{-1}, well below the width of 50 cm^{-1} that would indicate the simultaneous presence of both magnetite and maghemite (*51*). This observation suggests that insufficient quantities of magnetite had been oxidized into maghemite to be detectable via Raman spectroscopy. Alternatively, under the more reducing conditions at the distal end of the column, maghemite could have undergone reductive dissolution or autoreduction to magnetite, as suggested by others (*25*).

Additional Raman results similar to those depicted in Figure 2 were obtained for columns H−J. Mineral identifications for samples from these columns are summarized in Table 2, and representative Raman spectra may be found in the Supporting Information (Figures S3−S5). In general, the results presented in Table 2 indicate the extreme spatial variability of the mineral phases present within the iron columns. More highly oxidized phases (e.g., goethite, hematite) were typically found near the column inlet, and more reduced phases (e.g., green rust) were detected near the outlet. As was the case with column G, both magnetite and maghemite were detected within the proximal region of these columns, whereas only magnetite was detected in the distal portions. The prevalence of maghemite in the aged samples extracted near the influent end suggests that this mineral may be the ultimate oxidized corrosion product that forms within cast iron-based permeable reactive barriers.

Our prior studies (*9*) have shown that reactivity varies not only with position in a given column, but also varies temporally. To explain this phenomenon, we hypothesized that a passivation front moves through the column, with passivated (i.e., oxidized) regions near the influent and reactive (i.e., reduced) regions near the outlet. The existence of spatial variability in precipitate identity is consistent with this hypothesis. Based upon Raman analyses of sample grains extracted from two ports on column F at two different times (day 308 and day 921), it is also apparent that precipitate identity at a given port varies over time (Table 2; Figure S6). After 308 days, green rust was clearly present on the surface of grains extracted from port 2 but was absent from grains from port 1. After 921 days, however, the Raman bands indicating the presence of green rust had disappeared, leaving bands that correspond to goethite, magnetite, and maghemite. The conversion from redox-active precipitates such as green rusts to oxidized species such as goethite in this region clearly supports the existence of our hypothesized passivation front.

Precipitate Identification at Column Shutdown. XRD analysis of surficial phases from iron grains extracted from the influent end of all columns at shutdown (Figure S7) indicated that the main phases present were magnetite or maghemite, and a phase consistent with iron carbonate hydroxide (ICH, powder diffraction file 33-0650). ICH is a seldom-investigated corrosion product that forms at alkaline pH and has a hypothetical formula of $Fe^{2+}_{1.8}Fe^{3+}_{0.2}(OH)_{2.2}CO_3$ (*67*). Its characteristics are discussed in more detail below. The Raman spectrum of ICH has not been established, and this technique could therefore not be used to confirm the presence of ICH.

Green rust was not detected via XRD. The absence of green rust in the XRD samples cannot be attributed to oxidation during sample preparation or analysis, because samples of sulfate and carbonate green rust, prepared for

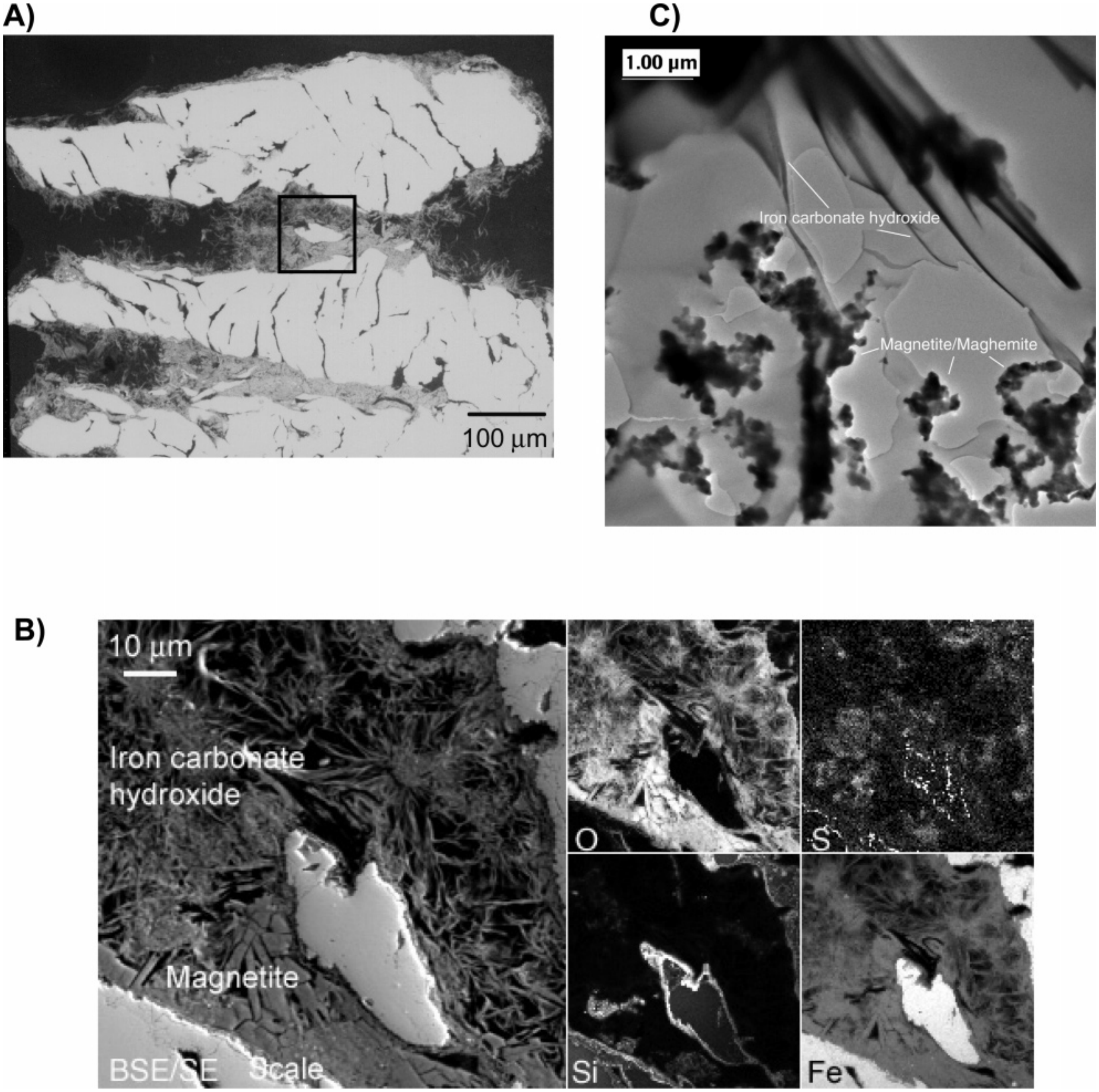

FIGURE 3. (A) SEM image of a cross-section through a reacted grain sample from the influent end of column D, taken after column shutdown. (B) Close-up of the indicated area of Figure 3A and elemental map of oxygen, iron, sulfur, and silicon. BSE/SE = backscattered/secondary electrons. Light colors indicate higher concentrations. (C) TEM image of iron carbonate hydroxide and magnetite/maghemite in a sample from the influent end of column J, taken after column shutdown.

XRD analysis under the same conditions, exhibited XRD patterns consistent with those described for these phases in ref *68*. Rather, our failure to identify green rust via XRD is likely to reflect spatial trends in precipitate formation. Raman results indicate green rust exists mainly near the effluent end of an aged column, whereas the iron grain samples for XRD analysis were obtained from the influent end of each column.

As compared to the unreacted grains, the relative amount of graphite and wüstite in the reacted grains has decreased and the fayalite peaks have disappeared in the XRD patterns (Figure S7). These phases may be unstable under our operating conditions and may have partially dissolved. Additionally, the sensitivity of the XRD instrument may have been insufficient to detect small amounts of wüstite and fayalite among other more prevalent mineral phases. As discussed below, TEM analysis confirmed the presence of fayalite in the exposed iron samples.

Amorphous or weakly crystalline iron (hydr)oxide or carbonate phases could also be present on our samples. For example, Furukawa and co-workers (*34*) found ferrihydrite in a majority of their samples. Because ferrihydrite crystallizes poorly, it is difficult to detect by XRD. Additionally, the primary Raman band for ferrihydrite is at 710 cm^{-1}, a region overlain by strong bands for magnetite and maghemite. SAED, however, should be able to record a diffraction pattern. In samples from columns D and J, no evidence of ferrihydrite was found by SAED. Amorphous phases, which can be identified by their lack of diffraction when investigated by SAED, were also not detected. This indicates that neither ferrihydrite nor amorphous phases were present as prominent constituents of our samples. Because SAED only considers a very small fraction of the sample, however, we cannot preclude their existence on a localized basis.

An SEM image (Figure 3A), a close-up, and a compositional map of a pore (Figure 3B) are shown for a sample from the influent end of column D, which was fed with 2 mM sodium bicarbonate and 100 μM of both TCE and 1,2,3-TCP during the majority of its lifetime. As for the unreacted grains, the images and elemental maps reveal the presence of MnS and silicon slag in all reacted grains (data not shown). The MnS slag appears to remain intact during exposure to solution, and little Mn is found in the oxide phase. A small amount of sulfur, however, was observed at the interface between the iron core and the oxide in some of the samples (Figure 3B). This result indicates that some sulfur may have dissolved and reprecipitated in conjunction with iron on top of the scale. Sulfur-containing iron minerals such as pyrite (FeS_2) (*17*), sulfate green rust ($[Fe_4^{2+}Fe_2^{3+}(OH)_{12}SO_4\cdot 4H_2O]$) (*19*), or iron sulfide (FeS) (*69*, *70*) have been shown to reduce organohalides. The iron/sulfur rims in these samples may thus represent a reactive entity.

Precipitate Layer Morphology. The oxide layer on the reacted grains is generally very thick, sometimes ranging to over 100 μm (Figure 3A), as compared to less than 2 μm on the raw grains (Figure 1B). Precipitates cover the entire grain, with the bare iron core never exposed. This finding suggests that reactions between contaminants and bare iron in corrosion pits, as hypothesized elsewhere (*71*), are unlikely to be the sole reactive site given the long diffusion paths that develop as the oxide layer grows.

The pores of the reacted grains (Figure 3A) generally contained substantial amounts of precipitates. Unlike the fresh grains, where the surficial layer mainly consisted of a single dense phase, the precipitates present on the exposed grains can be divided into at least three different types: the dense fayalite-containing scale, a compact, "blocky" phase, and a more porous phase consisting of "needles" or thin platelets. The three types of precipitates are easily discerned in the micrograph of the pore depicted in Figure 3B. From the compositional map of that region, the original grain boundary can be identified by the presence of the Si-rich scale.

To assign the three precipitate types characterized by SEM to their actual identities, a reacted iron sample was ion milled along the oxide/metal interface. The interface was analyzed via conventional TEM, SAED, and scanning transmission electron microscopy (STEM) collecting EDS X-ray maps. The dense, "blocky" structures determined using the microprobe appear as small grains on the TEM image (Figure 3C). SAED patterns of these regions identify these precipitates as either magnetite or maghemite; as with XRD, these phases cannot be distinguished by SAED alone.

TEM images obtained in addition to that shown in Figure 3C indicate that the porous structures have a hexagonal plate habit (not shown). Energy dispersive analysis (EDS) shows that both oxygen and iron are present in the platelets. It was not possible to analyze for H or C due to carbon coating and epoxy contamination, and there was little indication of chlorine present. The SAED patterns indicate this phase is distinctly different from magnetite or maghemite as well as from green rust (data not shown). On the basis of this information, we thus propose that the platelet structure corresponds to the iron carbonate hydroxide phase identified by XRD.

The Metal/Oxide Interface. Evidence of the original scale is still visible in the SEM images of most grains, but some regions in which the scale has degraded and transformed can be identified, as shown in Figure 4A. The degradation of the scale can be attributed to dissolution and reduction of the iron hydr(oxide) and iron silicate phases. Wüstite is unstable below 570 °C and readily decomposes to produce magnetite and Fe^0 (*48*). The dissolution of fayalite at alkaline pH, however, is expected to be slow (*72*). It thus appears that parts of the original scale undergo transformation into different iron-bearing phases. Furthermore, a thin gap of about 0.5 μm between the iron core and the scale is now apparent. This gap was not visible on the unreacted grains. Material thus seems to be dissolving from behind the Si-rich rim and ultimately reprecipitating on top of the original scale. A similar phenomenon can be seen in images of fresh and reacted commercial iron grains presented by Mackenzie and co-workers (*26*).

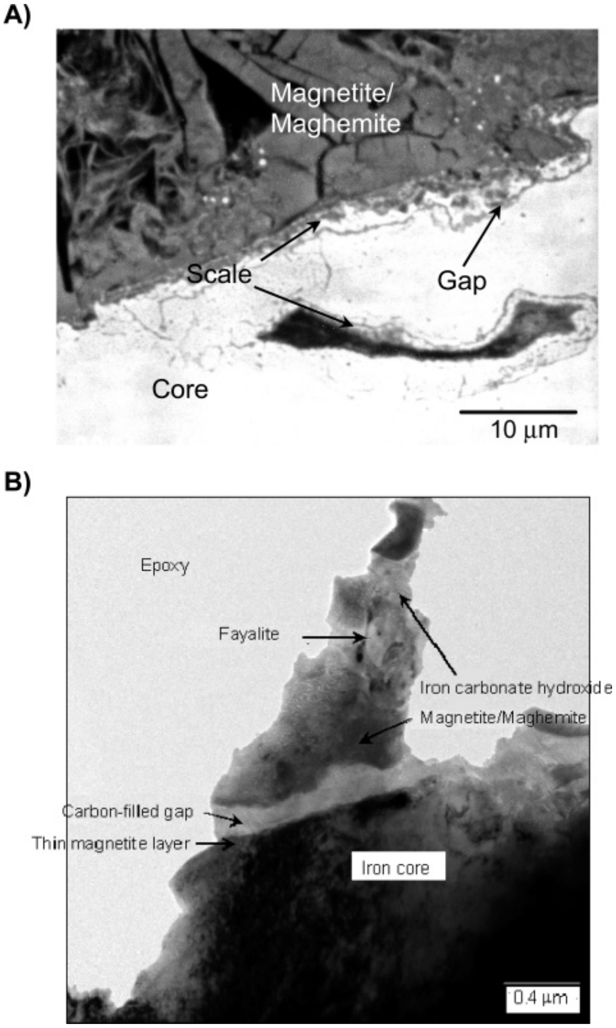

FIGURE 4. (A) SEM image of the degrading scale on a sample from the influent end of column D, taken after column shutdown. (B) TEM image of the metal/oxide interface.

TEM analysis of our samples shows that the nanometer scale texture of the metal/oxide interface exhibits a layered morphology (Figure 4B). In intimate contact with the metal is a very thin layer of nanocrystalline magnetite or maghemite. Adjacent to this nanocrystal layer, there is a gap filled with carbonaceous material. This material is probably part of the alteration structure and represents carbon associated with the metal after some of the iron has dissolved. The absence of a Cl signal in elemental maps of this gap (data not shown) indicates that the carbonaceous material is not an artifact originating from epoxy pore filling. The next layer contains a mixture of fayalite and magnetite/maghemite, with fayalite crystals (~200 nm) elongated roughly parallel to the interface. The magnetite/maghemite crystals are fine-grained (~50 nm) and mix with iron carbonate hydroxide platelets farther from the interface.

Characterization of Iron Carbonate Hydroxide. The XRD pattern of ICH is distinctly different from other iron carbonates, such as carbonate green rust or siderite (Figure S8). It does, however, resemble that of malachite ($Cu_2(OH)_2CO_3$),

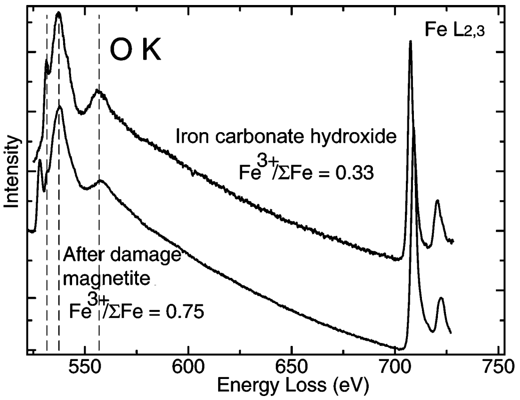

FIGURE 5. EELS spectra of iron carbonate hydroxide, before (top) and after (bottom) damage by the electron beam, showing the Fe $L_{2,3}$ and O K adsorption edges.

the structure of which can be described as octahedra of Cu^{2+} coordinated to oxygen or hydroxide anions, linked by carbonate to form chains (*73*). The similarity in XRD patterns suggests that iron carbonate hydroxide has the malachite structure and that it can be viewed as an iron malachite with Fe^{3+} hydroxide impurities (*67*).

To gain insight into the characteristics of iron carbonate hydroxide, the Fe $L_{2,3}$ and the O K adsorption edges were collected by EELS analysis (Figure 5). EELS is sensitive to the concentration, valence state, and bonding environment of atoms. Van Aken and co-workers (*74*) have developed an EELS/TEM method for determining the proportion of $Fe^{3+}/\Sigma Fe$ based upon analysis of the Fe $L_{2,3}$-edge spectra of several natural minerals and synthetic solutions. Using this technique, the EELS spectrum of a platelet was evaluated, and the $Fe^{3+}/\Sigma Fe$ ratio was estimated to be 0.33. This ratio is higher than expected (0.1) for the proposed iron hydroxide carbonate stoichiometry, but is lower than the ratio for magnetite or maghemite, and similar to that expected for carbonate green rust.

During the course of EELS analysis, it became apparent that the iron carbonate hydroxide platelets were damaged under the electron beam. Analysis of EELS spectra obtained after electron beam exposure revealed that the platelets had oxidized to an $Fe^{3+}/\Sigma Fe$ ratio of 0.75. This leads us to speculate that, although care was taken to minimize damage during the acquisition of EELS spectra, it is possible that the $Fe^{3+}/\Sigma Fe$ ratio is actually lower than measured. The change in the oxidation state is probably a result of the oxidation of iron carbonate hydroxide to an iron oxide, and the outgassing of CO_2 and water. The effects of this oxidation can be seen by the shift of the Fe $L_{2,3}$ adsorption edge to a higher energy loss, and the appearance of an oxygen pre-peak indicative of iron oxides (Figure 5; ref *74*). The SAED patterns of the damaged platelets are consistent with either maghemite or magnetite. The shape of the O K edge is also similar to either maghemite or magnetite. The observed amount of Fe^{3+}, however, is greater than in magnetite. We speculate that electron beam-induced damage of a platelet produces a partially oxidized magnetite structure.

Iron carbonate hydroxide has been observed by other researchers in studies of phases formed on field installation of PRBs (*14*). As a result of the lack of scrutiny that this phase has received, however, its existence for the most part has been overlooked. For example, Furakawa and co-workers (*34*) published an XRD pattern of precipitates obtained in a PRB used to remediate chlorinated solvents and hexavalent chromium that exhibits peaks around $2\theta = 14°, 17°$, and $24°$. These peaks are characteristic of iron carbonate hydroxide (see Figure S8), although this phase was not mentioned in that study.

Influence of Solution Composition−Silica. Although the presence of silica in the influent was previously shown to decrease the reactivity of the iron toward TCE (*9*, *75*), it did not significantly affect the morphology of the precipitated mineral structures (Figure 6A). The elemental map of an iron grain extracted from column B (fed with 2 mM $NaHCO_3$ and 10 mM NaCl over its entire operation period and 0.5 mM SiO_2 during the last 225 days of operation) reveals the presence of substantial amounts of silicon, not only in the original scale, but also in the newly formed oxide phase. A qualitative map of the Si/Fe ratio shows that the relative silicon content continuously increases from the core throughout the precipitate layer (Figure 6B). In contrast, the structurally similar precipitate phases of the columns that never received silica were depleted in silicon as compared to the iron core and original scale (see Figure 3B).

Several researchers have found that the presence of silica in solution leads to the formation of different iron hydr(oxide) phases as compared to silica-free solutions (*76*−*78*). This was not apparent in the present study; XRD and Raman analyses of samples from column B revealed the same mineral phases encountered in the other columns. It has to be noted, however, that column B was operated under silica-free conditions for the first 875 days (Table S1). A large fraction of the identified precipitates can thus be expected to have formed under silica-free conditions. The absence of additional precipitate phases indicates that silica sorbs onto the previously formed corrosion products without altering their identity. Furthermore, silica may precipitate as an amorphous phase not identifiable by the techniques employed in this study, or it may be present as impurities in the mineral phases identified by XRD and Raman.

Adsorption of silica onto or incorporation into newly formed precipitates can be inferred to cause the reduction in reactivity of the iron toward TCE. The inhibitory effect of silica can be viewed as the result of different processes (ref *79* and references therein). Silica is an anodic corrosion inhibitor that can form a protective layer consisting of a hydrated silica gel/iron (hydr)oxide mixture around the iron core. This layer prevents anodic dissolution of the iron ($Fe^0 \rightarrow Fe^{2+} + 2\ e^-$) and thereby hinders the transfer of electrons to the contaminant. Alternatively, adsorption of silica onto the precipitates can result in a shift in their surface potential, which may lead to reduced reactivity toward TCE.

Influence of Solution Composition−Bicarbonate. Our prior work (*9*) demonstrated that the column fed 20 mM sodium bicarbonate and 100 μM TCE/100 μM 1,2,3-TCP (column E) exhibited a substantial loss in iron reactivity toward TCE. Within 200 days, the reactivity had dropped to less than 10% of its original value. In comparing grains extracted from column E to those from columns fed 2 mM sodium bicarbonate (columns D and J), it is apparent that the grains from the high bicarbonate column were typically more extensively weathered (Supporting Information, Figure S9).

The weathering of the grains from column E was, however, highly heterogeneous, with some grains drastically weathered and others considerably less so. This result is consistent with the large amount of immobile water present within this column (*29*). With increased immobile water, the flow path heterogeneity would increase, and some grains would be in greater contact with the mobile phase than others.

On some of the iron grains from column E, the oxide layer was over 100 μm thick and at low magnification appeared as a solid phase under the microprobe. A close-up of the region, however, revealed that the oxide layer consisted of very closely packed, fine needles or plates of iron carbonate hydroxide, as can be seen on the left edge of the grain shown in Figure S9. Despite the abundant carbonate present, no siderite was detected by XRD in column E or any of the other

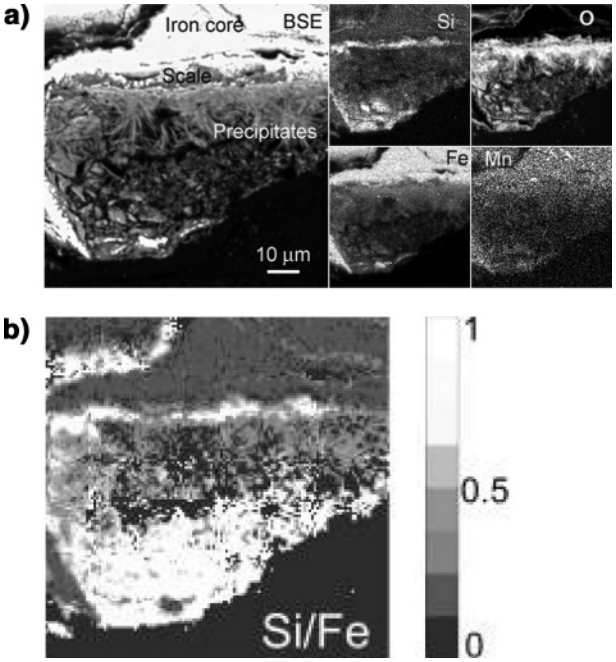

FIGURE 6. (A) SEM image and elemental map of oxygen, iron, manganese, and silicon of the precipitates on a grain from the influent end of column B, taken after column shutdown. BSE = backscattered electrons. Light colors indicate higher concentrations. (B) Qualitative map of the Si/Fe ratio. Light colors indicate higher ratios.

columns. The major sink of carbonate is therefore presumed to be iron carbonate hydroxide, the formation of which appears to have been enhanced by the presence of large amounts of bicarbonate.

Although the in-situ redox activity of iron carbonate hydroxide is unknown, its oxidation under the electron beam suggests that it is a redox-active phase that may be capable of reducing TCE. In addition, iron carbonate hydroxide may act as a conductor for electrons between the iron core and the contaminants. We speculate that if the precipitate layer becomes very thick, the distance for efficient electron transfer between iron core and contaminant becomes excessive, and iron carbonate hydroxide adopts an insulating capacity. The thickness of the overlayer between the interfacial region and the iron core thus may play an important role in the rate of electron transfer. Alternatively, the observed decrease in reactivity could signify that the precipitate layer functions as a barrier to diffusion of the contaminants.

Influence of Solution Composition−Calcium. Column G, which was fed with 2 mM CaCO$_3$ and 100 μM TCE/100 μM 1,2,3-TCP at pH 7.5, exhibited a progressive decrease in the dissolved calcium concentration along the column (data not shown). Interestingly, calcium retention did not lead to any perceptible passivation of the iron toward TCE relative to columns fed with NaHCO$_3$ at the same influent pH. This is in good agreement with a study by Vogan and co-workers (*6*), who found that the precipitation of calcite and aragonite from groundwater containing 5 mM bicarbonate or less did not lead to a discernible decrease in reactivity in a pilot scale PRB.

In the BSE/SE image (Supporting Information, Figure S10) of a sample from column G, it can be seen that the precipitate layer of the grain contains a number of dense, smooth chunks. The compositional map of this sample shows that these chunks contain calcium, but no iron. Calcium is not found in any other part of the oxide layer. XRD analysis revealed the presence of the usual iron corrosion products in this sample, along with calcite as the only calcium-bearing phase. Calcite covers only a small fraction of the overall surface, which may explain the lack of a measurable effect on iron reactivity.

The identity of the calcium-containing precipitates seems to vary from system to system. Some researchers have reported aragonite in field studies (*33*), aragonite in column studies and calcite in the field (*80*), or both phases in the same system (*6*, *12*). Aragonite was detected on the surface of our samples using micro-Raman spectroscopy (Table 2), but was not detected by XRD. Collectively, these measurements suggest that aragonite is a transitory phase that converted to calcite in the time that elapsed between the Raman and XRD analyses. This possibility is consistent with the known stability of the two phases and with reports for a field-scale PRB (*81*).

Corrosion Product Development

In our samples, the secondary corrosion products on the aged grains follow the sequence: original scale − magnetite/maghemite − iron carbonate hydroxide. This progression suggests that iron carbonate hydroxide is an intermediate corrosion product, which oxidizes to magnetite and ultimately maghemite over time. Additionally, within highly reactive portions of the column, green rust was detected. Green rust has been shown to transform to magnetite upon oxidation by nitrate (*82*) and carbon tetrachloride (*19*). We speculate that green rust and iron carbonate hydroxide are formed in parallel, depending on the local solution conditions within the pore space of the columns, and that they both convert to magnetite and maghemite over time. The mechanisms for these transformations probably involve dissolution of GR and ICH and neoformation of magnetite and/or maghemite. The transformation of green rust to iron carbonate hydroxide or vice versa is unlikely except for cases where the activity of CO$_2$ has changed.

Our results suggest that iron carbonate hydroxide is one of the major precipitates formed under conditions representative of PRBs. This phase is rarely mentioned in studies investigating corrosion products, perhaps because of the paucity of information about its characteristics. Further investigations regarding the formation and properties of iron carbonate hydroxide are needed, as it may constitute an important reactive species. In particular, its relationship to carbonate green rust and its potential to convert to more highly oxidized mineral phases need to be considered. Even though iron carbonate hydroxide is stable in air, our results indicate that it may be subject to oxidation in solution by contaminants such as TCE and may eventually be converted to magnetite and maghemite.

Acknowledgments

This material is based upon work supported by SERDP (contract CU-1125) and by the National Science Foundation (Grant No. CHE-0089168) as part of the Collaborative Research Activities in Environmental Molecular Science in Environmental Redox-Mediated Dehalogenation Chemistry at the Johns Hopkins University. The Johns Hopkins Electron Microbeam Facilities were established in part by grants from the Keck Foundation. The efforts of Jörg Klausen and William P. Ball during the initial years of these experiments are greatly appreciated. We would also like to thank Rick Wilkin for his valuable input on iron carbonate hydroxide, Michelle Scherer and Phil Larese-Casanova for kindly providing sulfate and carbonate green rust samples as XRD standards, and Markus Hilpert for helping with the computation of the Si/Fe ratios. Marek Odziemkowski and Robert Gillham of the University of Waterloo kindly provided access and support to facilitate our use of the micro-Raman instrument.

Supporting Information Available

Tables of the column operating conditions and XRD peak intensities; schematic of the experimental setup; figures containing XRD and Raman spectroscopic results from columns fed with various buffer compositions, showing spatial and temporal variability of precipitate phases; SEM image of a heavily reacted grain from column E (fed with 20 mM $NaHCO_3$); SEM image and elemental map of a sample from column G (fed with $CaCO_3$). This material is available free of charge via the Internet at http://pubs.acs.org.

Literature Cited

(1) Gillham, R. W.; O'Hannesin, S. F. Enhanced degradation of halogenated aliphatics by zerovalent iron. *Ground Water* **1994**, *32*, 958−967.

(2) Agrawal, A.; Tratnyek, P. G. Reduction of nitro aromatic compounds by zerovalent iron metal. *Environ. Sci. Technol.* **1996**, *30*, 153−160.

(3) Orth, W. S.; Gillham, R. W. Dechlorination of trichloroethene in aqueous solutions using Fe^0. *Environ. Sci. Technol.* **1996**, *30*, 66−71.

(4) Blowes, D. W.; Ptacek, C. J.; Jambor, J. L. In-situ remediation of Cr(VI)-contaminated groundwater using permeable reactive walls: Laboratory studies. *Environ. Sci. Technol.* **1997**, *31*, 3348−3357.

(5) Gu, B.; Liang, L.; Dickey, M. J.; Yin, X.; Dai, S. Reductive precipitation of uranium(VI) by zerovalent iron. *Environ. Sci. Technol.* **1998**, *32*, 3366−3373.

(6) Vogan, J. L.; Focht, R. M.; Clark, P.; Graham, M. J. Performance evaluation of a permeable reactive barrier for remediation of dissolved chlorinated solvents in groundwater. *J. Hazard. Mater.* **1999**, *68*, 97−108.

(7) Klausen, J.; Ranke, J.; Schwarzenbach, R. P. Influence of solution composition and column aging on the reduction of nitroaromatic compounds by zerovalent iron. *Chemosphere* **2001**, *44*, 511−517.

(8) Su, C.; Puls, R. W. Arsenate and arsenite removal by zerovalent iron: kinetics, redox transformation, and implications for in situ groundwater remediation. *Environ. Sci. Technol.* **2001**, *35*, 4562−4568.

(9) Klausen, J.; Vikesland, P. J.; Kohn, T.; Burris, D. R.; Ball, W. P.; Roberts, A. L. Longevity of cast iron in groundwater treatment processes: solution composition effects on reactivity towards organohalides and nitroaromatic compounds. *Environ. Sci. Technol.* **2003**, *37*, 1208−1218.

(10) Dixit, S.; Hering, J. G. Comparison of arsenic(V) and arsenic(III) sorption onto iron oxide minerals: implications for arsenic mobility. *Environ. Sci. Technol.* **2003**, *37*, 4182−1189.

(11) Gu, B.; Phelps, T. J.; Liang, L.; Dickey, M. J.; Roh, Y.; Kinsall, B. L.; Palumbo, A. V.; Jacobs, G. K. Biogeochemical dynamics in zerovalent iron columns: Implications for permeable reactive barriers. *Environ. Sci. Technol.* **1999**, *33*, 2170−2177.

(12) Roh, Y.; Lee, S. Y.; Elless, M. P. Characterization of corrosion products in the permeable reactive barriers. *Environ. Geol.* **2000**, *40*, 184−194.

(13) Kamolpornwijit, W.; Liang, L.; West, O. R.; Moline, G. R.; Sullivan, A. B. Preferential flow path development and its influence on long-term PRB performance: column study. *J. Contam. Hydrol.* **2003**, *66*, 161−178.

(14) Wilkin, R. T.; Puls, R. W. *Capstone Report on the Application, Monitoring, and Performance of Permeable Reactive Barriers for Ground Water Remediation*; U.S. Environmental Protection Agency, Office of Research and Development: Cincinnati, OH, 2003; EPA/600/R-03/045a.

(15) Oh, S. Y.; Cha, D. K.; Chiu, P. C. Graphite-mediated reduction of 2,3-dinitrotoluene with elemental iron. *Environ. Sci. Technol.* **2002**, *36*, 2178−2184.

(16) Sivavec, T. M.; Horney, D. P. Reduction of chlorinated solvents by iron(II) minerals. *Abstract of Papers*; 213th National Meeting of the American Chemical Society: San Francisco, CA, 1997; Vol. 37, pp 115−117.

(17) Lee, W.; Batchelor, B. Abiotic reductive dechlorination of chlorinated ethylenes by iron-bearing soil minerals. 1. Pyrite and magnetite. *Environ. Sci. Technol.* **2002**, *36*, 5147−5154.

(18) Gregory, K. B.; Larese-Casanova, P.; Parkin, G. F.; Scherer, M. M. Abiotic transformation of hexahydro-1,3,5-trinitro-1,3,5-triazine by Fe^{II} bound to magnetite. *Environ. Sci. Technol.* **2004**, *38*, 1408−1414.

(19) Erbs, M.; Bruun, H. C.; Olsen, C. E. Reductive dechlorination of carbon tetrachloride using iron(II) iron(III) hydroxide sulfate (green rust). *Environ. Sci. Technol.* **1999**, *33*, 307−311.

(20) Lee, W.; Batchelor, B. Abiotic reductive dechlorination of chlorinated ethylenes by iron-bearing soil minerals. 2. Green rust. *Environ. Sci. Technol.* **2002**, *36*, 5348−5354.

(21) Klausen, J.; Tröber, S. P.; Haderlein, S. B.; Schwarzenbach, R. P. Reduction of substituted nitrobenzenes by Fe(II) in aqueous mineral suspensions. *Environ. Sci. Technol.* **1995**, *29*, 2396−2404.

(22) Amonette, J. E.; Workman, D. J.; Kennedy, D. W.; Fruchter, J. S.; Gorby, Y. A. Dechlorination of carbon tetrachloride by Fe(II) associated with goethite. *Environ. Sci. Technol.* **2000**, *34*, 4606−4613.

(23) Pecher, K.; Haderlein, S. B.; Schwarzenbach, R. P. Reduction of polyhalogenated methanes by surface-bound Fe(II) in aqueous suspension of iron oxides. *Environ. Sci. Technol.* **2002**, *36*, 1734−1741.

(24) Elsner, M.; Schwarzenbach, R. P.; Haderlein, S. B. Reactivity of Fe(II)-bearing minerals toward reductive transformation of organic contaminants. *Environ. Sci. Technol.* **2004**, *38*, 799−807.

(25) Ritter, K.; Odziemkowski, M. S.; Gillham, R. W. An in-situ study of the role of surface films on granular iron in the permeable iron wall technology. *J. Contam. Hydrol.* **2002**, *55*, 87−111.

(26) Mackenzie, P. D.; Horney, D. P.; Sivavec, T. M. Mineral precipitation and porosity losses in granular iron columns. *J. Hazard. Mater.* **1999**, *68*, 1−17.

(27) Liang, L.; Korte, N.; Gu, B.; Puls, R. W.; Reeter, C. Geochemical and microbial reactions affecting the long-term performance of in situ 'iron barriers'. *Adv. Environ. Res.* **2000**, *4*, 273−286.

(28) Wilkin, R. T.; Puls, R. W.; Sewell, G. W. *Long-Term Performance of Permeable Reactive Barriers Using Zerovalent Iron: An Evaluation at Two Sites*; U.S. EPA, National Risk Management Research Laboratory: Cincinnati, OH, 2002; EPA/600/S-02/001.

(29) Vikesland, P. J.; Klausen, J.; Zimmermann, H.; Roberts, A. L.; Ball, W. P. Longevity of cast iron in groundwater treatment processes: changes in solute transport properties over time. *J. Contam. Hydrol.* **2003**, *64*, 3−33.

(30) Yabusaki, S.; Cantrell, K.; Sass, B.; Steefel, C. Multicomponent reactive transport in an in situ zerovalent iron cell. *Environ. Sci. Technol.* **2001**, *35*, 1493−1503.

(31) Gui, J.; Devine, T. M. A SERS investigation of the passive films formed on iron in mildly alkaline solutions of carbonate/bicarbonate and nitrate. *Corros. Sci.* **1995**, *37*, 1177−1189.

(32) Odziemkowski, M. S.; Schuhmacher, T. T.; Gillham, R. W.; Reardon, E. J. Mechanism of oxide film formation on iron in simulating groundwater solutions: Raman spectroscopic studies. *Corros. Sci.* **1998**, *40*, 371−389.

(33) Phillips, D. H.; Gu, B.; Watson, D. B.; Roh, Y.; Liang, L.; Lee, S. Y. Performance evaluation of a zerovalent iron reactive barrier: mineralogical characteristics. *Environ. Sci. Technol.* **2000**, *34*, 4169−4176.

(34) Furukawa, Y.; Kim, J.-W.; Watkins, J.; Wilkin, R. T. Formation of ferrihydrite and associated iron corrosion products in permeable reactive barriers of zerovalent iron. *Environ. Sci. Technol.* **2002**, *36*, 5469−5475.

(35) Köber, R.; Schlicker, O.; Ebert, M.; Dahmke, A. Degradation of chlorinated ethylenes by Fe(0): inhibition processes and mineral precipitation. *Environ. Geol.* **2002**, *41*, 644−652.

(36) Egerton, R. F. *Electron Energy-loss Spectroscopy in the Electron Microscope*; Plenum: New York, 1996.

(37) Dunnwald, J.; Otto, A. An Investigation of phase-transitions in rust layers using Raman-spectroscopy. *Corros. Sci.* **1989**, *29*, 1167−1176.

(38) Chawla, S. L.; Gupta, R. K. *Materials Selection for Corrosion Control*; ASM International: Materials Park, OH, 1993.

(39) Burris, D. R.; Campbell, T. J.; Manoranjan, V. S. Sorption of trichloroethylene and tetrachloroethylene in a batch reactive metallic iron-water system. *Environ. Sci. Technol.* **1995**, *29*, 2850−2855.

(40) Deng, B.; Campbell, T. J.; Burris, D. R. Hydrocarbon formation in metallic iron/water system. *Environ. Sci. Technol.* **1997**, *31*, 1185−1190.

(41) Landis, R. L.; Gillham, R. W.; Reardon, E. J.; Fagan, R.; Focht, R. M.; Vogan, J. L. An examination of zerovalent iron sources used in permeable reactive barriers. *Proceedings of the 2001*

International Containment and Remediation Technology Conference and Exhibition; Orlando, FL, 2001.

(42) Ryan, M. P.; Williams, D. E.; Chater, R. J.; Hutton, B. M.; McPhail, D. S. Why stainless steel corrodes. *Nature* **2002**, *415*, 770−774.

(43) Gaspar, D. J.; Lea, A. S.; Engelhard, M. H.; Baer, D. R.; Miehr, R.; Tratnyek, P. G. Evidence for localization of reaction upon reduction of carbon-tetrachloride by granular iron. *Langmuir* **2002**, *18*, 7688−7693.

(44) Burke, D. P.; Higginson, R. L. Characterization of multicomponent scales by electron backscattered diffraction (EBSD). *Scr. Mater.* **2000**, *42*, 277−281.

(45) Jenko, M.; Korousic, B.; Mandrino, D.; Presern, V. HRAES study of oxide scale formation by decarburization of nonoriented electrical steel sheets. *Vacuum* **2000**, *57*, 295−305.

(46) Taniguchi, S.; Yamamoto, K.; Megumi, D.; Shibata, T. Characteristics of scale/ substrate interface area of Si-containing low-carbon steels at high temperatures. *Mater. Sci. Eng., A* **2001**, *A308*, 250−257.

(47) Odziemkowski, M. S.; Gillham, R. S. Surface redox reactions on commercial grade granular iron (steel) and their influence on the reductive dechlorination of solvent. Micro Raman spectroscopic studies. *Abstract of Papers*; 213th National Meeting of the American Chemical Society: San Francisco, CA, 1997; Vol. 37(1), pp 177−180.

(48) de Faria, D. L. A.; Venâncio Silva, S.; de Oliveira, M. T. Raman microspectroscopy of some iron oxides and oxyhydroxides. *J. Raman Spectrosc.* **1997**, *28*, 873−878.

(49) Shebanova, O. N.; Lazor, P. Raman spectroscopic study of magnetite ($FeFe_2O_4$): a new assignment for the vibrational spectrum. *J. Solid State Chem.* **2003**, *174*, 424−430.

(50) Shebanova, O. N.; Lazor, P. Raman study of magnetite (Fe_3O_4): laser-induced thermal effects and oxidation. *J. Raman Spectrosc.* **2003**, *34*, 845−852.

(51) Odziemkowski, M. S.; Flis, J.; Irish, D. E. Raman spectral and electrochemical studies of surface-film formation on iron and its alloys with carbon in $Na_2CO_3/NaHCO_3$ solution with reference to stress-corrosion cracking. *Electrochim. Acta* **1994**, *39*, 2225−2236.

(52) Jolivet, J. P.; Tronc, E. Interfacial electron-transfer in colloidal spinel iron-oxide − conversion of Fe_3O_4−Gamma-Fe_2O_3 in Aqueous-Medium. *J. Colloid Interface Sci.* **1988**, *125*, 688−701.

(53) Tang, J.; Myers, M.; Bosnick, K. A.; Brus, L. E. Magnetite Fe_3O_4 nanocrystals: Spectroscopic observation of aqueous oxidation kinetics. *J. Phys. Chem. B* **2003**, *107*, 7501−7506.

(54) Peterson, M. L.; Brown, G. E.; Parks, G. A. Direct XAFS evidence for heterogeneous redox reaction at the aqueous chromium/ magnetite interface. *Colloids Surf., A* **1996**, *107*, 77−88.

(55) Peterson, M. L.; White, A. F.; Brown, G. E.; Parks, G. A. Surface passivation of magnetite by reaction with aqueous Cr(VI): XAFS and TEM results. *Environ. Sci. Technol.* **1997**, *31*, 1573−1576.

(56) Jolivet, J. P.; Tronc, E.; Barbe, C.; Livage, J. Interfacial electron transfer in colloidal spinel iron oxide: Silver ion reduction in aqueous medium. *J. Colloid Interface Sci.* **1990**, *138*, 465−472.

(57) McCormick, M. L.; Bouwer, E. J.; Adriaens, P. Carbon tetrachloride transformation in a model iron-reducing culture: Relative kinetics of biotic and abiotic reactions. *Environ. Sci. Technol.* **2002**, *36*, 403−410.

(58) Danielsen, K.; Hayes, K. F. Base enhanced dechlorination of carbon tetrachloride by magnetite. *Abstract of Papers*; 225th National Meeting of the American Chemical Society: New Orleans, LA, 2003; Vol. 43, pp 576−581.

(59) Sidhu, P. S.; Gilkes, R. J.; Posner, A. M. Mechanism of the low temperature oxidation of synthetic magnetites. *J. Inorg. Nucl. Chem.* **1977**, *39*, 1953−1958.

(60) Bonin, P. M. L.; Odziemkowski, M. S.; Reardon, E. J.; Gillham, R. W. *In Situ* identification of carbonate-containing green rust on iron electrodes in solutions simulating groundwater. *J. Solution Chem.* **2000**, *29*, 1061−1074.

(61) Herman, R. G.; Bodgan, C. E.; Sommer, A. J.; Simpson, D. R. Discrimination among carbonate minerals by Raman spectroscopy using the laser microprobe. *Appl. Spectrosc.* **1987**, *41*, 437−440.

(62) Boucherit, N.; Hugot-Le Goff, A.; Joiret, S. Raman studies of corrosion films grown on Fe and Fe-6Mo in pitting conditions. *Corros. Sci.* **1991**, *32*, 497−507.

(63) Legrand, L.; Sagon, G.; Lecomte, S.; Chausse, A.; Messina, R. A Raman and infrared study of a new carbonate green rust obtained by electrochemical way. *Corros. Sci.* **2001**, *43*, 1739−1749.

(64) Refait, P.; Abdelmoula, M.; Génin, J.-M. R. Mechanisms of formation and structure of green rust one in aqueous corrosion of iron in the presence of chloride ions. *Corros. Sci.* **1998**, *40*, 1547−1560.

(65) Abdelmoula, M.; Refait, P.; Drissi, S. H.; Mihe, J. P.; Génin, J.-M. R. Conversion electron Mössbauer spectroscopy and X-ray diffraction studies of the formation of carbonate-containing green rust one by corrosion of metallic iron in $NaHCO_3$ and ($NaHCO_3$ + NaCl) solutions. *Corros. Sci.* **1996**, *38*, 623−633.

(66) Simard, S.; Odziemkowski, M.; Irish, D. E.; Brossard, L.; Ménard, H. *In Situ* micro-Raman spectroscopy to investigate pitting corrosion product of 1024 mild steel in phosphate and bicarbonate solutions containing chloride and sulfate ions. *J. Appl. Electrochem.* **2001**, *31*, 931−920.

(67) Erdös, E.; Altorfer, H. Ein dem Malachit aehnliches basisches Eisenkarbonat als Korrosionsprodukt von Stahl. *Werkst. Korros.* **1976**, *27*, 304−312.

(68) Williams, A. G. B.; Scherer, M. M. Kinetics of Cr(VI) reduction by carbonate green rust. *Environ. Sci. Technol.* **2001**, *35*, 3488−3494.

(69) Butler, E. C.; Hayes, K. F. Kinetics of the transformation of trichloroethylene and tetrachloroethylene by iron sulfide. *Environ. Sci. Technol.* **1999**, *33*, 2021−2027.

(70) Butler, B. J.; Hayes, K. F. Kinetics of the transformation of halogenated aliphatic compounds by iron sulfide. *Environ. Sci. Technol.* **2000**, *34*, 422−429.

(71) Scherer, M. M.; Balko, B. A.; Tratnyek, P. G. The Role of Oxides in Reduction Reactions at the Metal-Water Interface. In *Mineral-Water Interfacial Reactions. Kinetics and Mechanisms*; Sparks, D. L., Grundl, T. J., Eds.; American Chemical Society: Washington, DC, 1999; pp 301−322.

(72) Wogelius, R. A.; Walther, J. V. Olivine dissolution kinetics at near-surface conditions. *Chem. Geol.* **1992**, *97*, 101−112.

(73) MineralWeb, http://www.minweb.co.uk; accessed February 2004.

(74) van Aken, P. A.; Liebscher, B.; Styrsa, V. J. Quantitative determination of iron oxidation states in minerals using Fe $L_{2,3}$-edge electron energy-loss near-edge structure spectroscopy. *Phys. Chem. Miner.* **1998**, *25*, 323−327.

(75) Kohn, T.; Roberts, A. L. The effect of silica on the degradation of organohalides in granular iron columns. *J. Contam. Hydrol.*, submitted.

(76) Hansen, H. C. B.; Wetche, T. P.; Raulundrasmussen, K.; Borggaard, O. K. Stability-constants for silicate adsorbed to ferrihydrite. *Clay Miner.* **1994**, *29*, 341−350.

(77) Anderson, P. R.; Benjamin, M. M. Effects of silicon on the crystallization and adsorption properties of ferric oxides. *Environ. Sci. Technol.* **1985**, *19*, 1048−1053.

(78) Mayer, T. D.; Jarrell, W. M. Formation and stability of iron(II) oxidation products under natural concentrations of dissolved silica. *Water Res.* **1996**, *30*, 1208−1214.

(79) Kohn, T.; Kane, S. R.; Fairbrother, D. H.; Roberts, A. L. Investigation of the inhibitory effect of silica on the degradation of 1,1,1-trichloroethane by granular iron. *Environ. Sci. Technol.* **2003**, *37*, 5806−5812.

(80) Sass, B., personal communication.

(81) Phillips, D. H.; Watson, D. B.; Roh, Y.; Gu, B. Mineralogical characteristics and transformations during long-term operation of a zerovalent iron reactive barrier. *J. Environ. Qual.* **2003**, *32*, 2033−2045.

(82) Hansen, H. C. B.; Koch, C. B.; Nancke-Krogh, H.; Borggaard, O. K.; Sørensen, J. Abiotic nitrate reduction to ammonium: key role of green rust. *Environ. Sci. Technol.* **1996**, *30*, 2053−2056.

(83) Ohtsuka, T.; Kubo, K.; Sato, N. Raman spectroscopy of thin corrosion films on iron at 100 to 150 °C in air. *Corrosion* **1986**, *42*, 476−482.

(84) Thierry, D.; Persson, D.; Leygraf, C.; Boucherit, N.; Hugot-LeGoff, A. Raman-spectroscopy and XPS investigations of anodic corrosion films formed on Fe−Mo alloys in Alkaline-Solutions. *Corros. Sci.* **1991**, *32*, 273.

(85) Mazzetti, L.; Thistlethwaite, P. J. Raman spectra and thermal transformations of ferrihydrite and schwertmannite. *J. Raman Spectrosc.* **2002**, *33*, 104−111.

(86) Simpson, L. J. Electrochemically generated $CaCO_3$ deposits on iron studied with FTIR and Raman spectroscopy. *Electrochim. Acta* **1998**, *43*, 2543−2547.

(87) Gout, R.; Oelkers, E. H.; Schott, J.; Zwick, A. The surface chemistry and structure of acid-leached albite: New insights on the dissolution mechanism of the alkali feldspars. *Geochim. Cosmochim. Acta* **1997**, *61*, 3013−3018.

(88) Chopelas, A. Single-crystal Raman-spectra of forsterite, fayalite, and monticellite. *Am. Mineral.* **1991**, *76*, 1101−1109.

(89) Bonin, P. M. L.; Jedral, W.; Odziemkowski, M. S.; Gillham, R. W. Electrochemical and Raman spectroscopic studies of the influence of chlorinated solvents on the corrosion behavior of iron in borate buffer and in simulated groundwater. *Corros. Sci.* **2000**, *42*, 1921−1939.

(90) Ferrari, A. C.; Robertson, J. Resonant Raman spectroscopy of disordered, amorphous, and diamondlike carbon. *Phys. Rev. B* **2001**, 6407.

Received for review July 23, 2004. Revised manuscript received December 28, 2004. Accepted January 3, 2005.

ES048851K